

DESY-99-058

# Search for Contact Interactions in Deep Inelastic $e^+p \rightarrow e^+X$ Scattering at HERA

ZEUS Collaboration

## Abstract

In a search for signatures of physics processes beyond the Standard Model, various  $eeqq$  vector contact-interaction hypotheses have been tested using the high- $Q^2$ , deep inelastic neutral-current  $e^+p$  scattering data collected with the ZEUS detector at HERA. The data correspond to an integrated luminosity of  $47.7 \text{ pb}^{-1}$  of  $e^+p$  interactions at  $300 \text{ GeV}$  center-of-mass energy. No significant evidence of a contact-interaction signal has been found. Limits at the 95% confidence level are set on the contact-interaction amplitudes. The effective mass scales  $\Lambda$  corresponding to these limits range from  $1.7 \text{ TeV}$  to  $5 \text{ TeV}$  for the contact-interaction scenarios considered.

# The ZEUS Collaboration

J. Breitweg, S. Chekanov, M. Derrick, D. Krakauer, S. Magill, B. Musgrave,  
A. Pellegrino, J. Repond, R. Stanek, R. Yoshida

*Argonne National Laboratory, Argonne, IL, USA* <sup>p</sup>

M.C.K. Mattingly

*Andrews University, Berrien Springs, MI, USA*

G. Abbiendi, F. Anselmo, P. Antonioli, G. Bari, M. Basile, L. Bellagamba,  
D. Boscherini<sup>1</sup>, A. Bruni, G. Bruni, G. Cara Romeo, G. Castellini<sup>2</sup>, L. Cifarelli<sup>3</sup>,  
F. Cindolo, A. Contin, N. Coppola, M. Corradi, S. De Pasquale, P. Giusti,  
G. Iacobucci<sup>4</sup>, G. Laurenti, G. Levi, A. Margotti, T. Massam, R. Nania, F. Palmonari,  
A. Pesci, A. Polini, G. Sartorelli, Y. Zamora Garcia<sup>5</sup>, A. Zichichi  
*University and INFN Bologna, Bologna, Italy* <sup>f</sup>

C. Amelung, A. Bornheim, I. Brock, K. Coböken, J. Crittenden, R. Deffner, M. Eckert<sup>6</sup>,  
H. Hartmann, K. Heinloth, L. Heinz<sup>7</sup>, E. Hilger, H.-P. Jakob, A. Kappes, U.F. Katz,  
R. Kerger, E. Paul, M. Pfeiffer<sup>8</sup>, J. Rautenberg, H. Schnurbusch, A. Stifutkin,  
J. Tandler, A. Weber, H. Wieber

*Physikalisches Institut der Universität Bonn, Bonn, Germany* <sup>c</sup>

D.S. Bailey, O. Barret, W.N. Cottingham, B. Foster<sup>9</sup>, G.P. Heath, H.F. Heath,  
J.D. McFall, D. Piccioni, J. Scott, R.J. Tapper

*H.H. Wills Physics Laboratory, University of Bristol, Bristol, U.K.* <sup>o</sup>

M. Capua, A. Mastroberardino, M. Schioppa, G. Susinno

*Calabria University, Physics Dept. and INFN, Cosenza, Italy* <sup>f</sup>

H.Y. Jeoung, J.Y. Kim, J.H. Lee, I.T. Lim, K.J. Ma, M.Y. Pac<sup>10</sup>

*Chonnam National University, Kwangju, Korea* <sup>h</sup>

A. Caldwell, N. Cartiglia, Z. Jing, W. Liu, B. Mellado, J.A. Parsons, S. Ritz<sup>11</sup>,  
R. Sacchi, S. Sampson, F. Sciulli, Q. Zhu<sup>12</sup>

*Columbia University, Nevis Labs., Irvington on Hudson, N.Y., USA* <sup>q</sup>

P. Borzemski, J. Chwastowski, A. Eskreys, J. Figiel, K. Klimek, K. Olkiewicz,  
M.B. Przybycień, L. Zawiejski

*Inst. of Nuclear Physics, Cracow, Poland* <sup>j</sup>

L. Adamczyk<sup>13</sup>, B. Bednarek, K. Jeleń, D. Kisielewska, A.M. Kowal, T. Kowalski,  
M. Przybycień, E. Rulikowska-Zarębska, L. Suszycki, J. Zając

*Faculty of Physics and Nuclear Techniques, Academy of Mining and Metallurgy, Cracow,  
Poland* <sup>j</sup>

Z. Duliński, A. Kotański

*Jagellonian Univ., Dept. of Physics, Cracow, Poland <sup>k</sup>*

L.A.T. Bauerdtick, U. Behrens, J.K. Bienlein, C. Burgard, K. Desler, G. Drews,  
A. Fox-Murphy, U. Fricke, F. Goebel, P. Göttlicher, R. Graciani, T. Haas, W. Hain,  
G.F. Hartner, D. Hasell<sup>14</sup>, K. Hebbel, K.F. Johnson<sup>15</sup>, M. Kasemann<sup>16</sup>, W. Koch,  
U. Kötz, H. Kowalski, L. Lindemann, B. Löhr, M. Martínez, J. Milewski<sup>17</sup>, M. Milite,  
T. Monteiro<sup>18</sup>, M. Moritz, D. Notz, F. Pelucchi, K. Piotrzkowski, M. Rohde,  
P.R.B. Saull, A.A. Savin, U. Schneekloth, O. Schwarzer<sup>19</sup>, F. Selonke, M. Sievers,  
S. Stonjek, E. Tassi, G. Wolf, U. Wollmer, C. Youngman, W. Zeuner

*Deutsches Elektronen-Synchrotron DESY, Hamburg, Germany*

B.D. Burow<sup>20</sup>, C. Coldewey, H.J. Grabosch, A. Lopez-Duran Viani, A. Meyer,  
K. Mönig, S. Schlenstedt, P.B. Straub

*DESY Zeuthen, Zeuthen, Germany*

G. Barbagli, E. Gallo, P. Pelfer

*University and INFN, Florence, Italy <sup>f</sup>*

G. Maccarrone, L. Votano

*INFN, Laboratori Nazionali di Frascati, Frascati, Italy <sup>f</sup>*

A. Bamberger, S. Eisenhardt<sup>21</sup>, P. Markun, H. Raach, S. Wölfle

*Fakultät für Physik der Universität Freiburg i.Br., Freiburg i.Br., Germany <sup>c</sup>*

N.H. Brook<sup>22</sup>, P.J. Bussey, A.T. Doyle, S.W. Lee, N. Macdonald, G.J. McCance,  
D.H. Saxon, L.E. Sinclair, I.O. Skillicorn, E. Strickland, R. Waugh

*Dept. of Physics and Astronomy, University of Glasgow, Glasgow, U.K. <sup>o</sup>*

I. Bohnet, N. Gendner, U. Holm, A. Meyer-Larsen, H. Salehi, K. Wick

*Hamburg University, I. Institute of Exp. Physics, Hamburg, Germany <sup>c</sup>*

A. Garfagnini, I. Gialas<sup>23</sup>, L.K. Gladilin<sup>24</sup>, D. Kçira<sup>25</sup>, R. Klanner, E. Lohrmann,  
G. Poelz, F. Zetsche

*Hamburg University, II. Institute of Exp. Physics, Hamburg, Germany <sup>c</sup>*

T.C. Bacon, J.E. Cole, G. Howell, L. Lamberti<sup>26</sup>, K.R. Long, D.B. Miller, A. Prinias<sup>27</sup>,  
J.K. Sedgbeer, D. Sideris, A.D. Tapper, R. Walker

*Imperial College London, High Energy Nuclear Physics Group, London, U.K. <sup>o</sup>*

U. Mallik, S.M. Wang

*University of Iowa, Physics and Astronomy Dept., Iowa City, USA <sup>p</sup>*

P. Cloth, D. Filges

*Forschungszentrum Jülich, Institut für Kernphysik, Jülich, Germany*

T. Ishii, M. Kuze, I. Suzuki<sup>28</sup>, K. Tokushuku<sup>29</sup>, S. Yamada, K. Yamauchi, Y. Yamazaki  
*Institute of Particle and Nuclear Studies, KEK, Tsukuba, Japan*<sup>g</sup>

S.H. Ahn, S.H. An, S.J. Hong, S.B. Lee, S.W. Nam<sup>30</sup>, S.K. Park  
*Korea University, Seoul, Korea*<sup>h</sup>

H. Lim, I.H. Park, D. Son  
*Kyungpook National University, Taegu, Korea*<sup>h</sup>

F. Barreiro, J.P. Fernández, G. García, C. Glasman<sup>31</sup>, J.M. Hernández<sup>32</sup>, L. Labarga,  
J. del Peso, J. Puga, I. Redondo<sup>33</sup>, J. Terrón  
*Univer. Autónoma Madrid, Depto de Física Teórica, Madrid, Spain*<sup>n</sup>

F. Corriveau, D.S. Hanna, J. Hartmann<sup>34</sup>, W.N. Murray<sup>6</sup>, A. Ochs, S. Padhi,  
M. Riveline, D.G. Stairs, M. St-Laurent, M. Wing  
*McGill University, Dept. of Physics, Montréal, Québec, Canada*<sup>a</sup>, <sup>b</sup>

T. Tsurugai  
*Meiji Gakuin University, Faculty of General Education, Yokohama, Japan*

V. Bashkirov<sup>35</sup>, B.A. Dolgoshein  
*Moscow Engineering Physics Institute, Moscow, Russia*<sup>l</sup>

G.L. Bashindzhagyan, P.F. Ermolov, Yu.A. Golubkov, L.A. Khein, N.A. Korotkova,  
I.A. Korzhavina, V.A. Kuzmin, O.Yu. Lukina, A.S. Proskuryakov, L.M. Shcheglova<sup>36</sup>,  
A.N. Solomin<sup>36</sup>, S.A. Zotkin  
*Moscow State University, Institute of Nuclear Physics, Moscow, Russia*<sup>m</sup>

C. Bokel, M. Botje, N. Brümmer, J. Engelen, E. Koffeman, P. Kooijman, A. van Sighem,  
H. Tiecke, N. Tuning, J.J. Velthuis, W. Verkerke, J. Vossebeld, L. Wiggers, E. de Wolf  
*NIKHEF and University of Amsterdam, Amsterdam, Netherlands*<sup>i</sup>

D. Acosta<sup>37</sup>, B. Bylsma, L.S. Durkin, J. Gilmore, C.M. Ginsburg, C.L. Kim, T.Y. Ling,  
P. Nylander  
*Ohio State University, Physics Department, Columbus, Ohio, USA*<sup>p</sup>

H.E. Blaikley, S. Boogert, R.J. Cashmore<sup>18</sup>, A.M. Cooper-Sarkar, R.C.E. Devenish,  
J.K. Edmonds, J. Große-Knetter<sup>38</sup>, N. Harnew, T. Matsushita, V.A. Noyes<sup>39</sup>,  
A. Quadt<sup>18</sup>, O. Ruske, M.R. Sutton, R. Walczak, D.S. Waters  
*Department of Physics, University of Oxford, Oxford, U.K.*<sup>o</sup>

A. Bertolin, R. Brugnera, R. Carlin, F. Dal Corso, S. Dondana, U. Dosselli, S. Dusini,  
S. Limentani, M. Morandin, M. Posocco, L. Stanco, R. Stroili, C. Voci  
*Dipartimento di Fisica dell' Università and INFN, Padova, Italy*<sup>f</sup>

L. Iannotti<sup>40</sup>, B.Y. Oh, J.R. Okrasinski, W.S. Toothacker, J.J. Whitmore  
*Pennsylvania State University, Dept. of Physics, University Park, PA, USA*<sup>q</sup>

Y. Iga

*Polytechnic University, Sagamihara, Japan* <sup>g</sup>

G. D'Agostini, G. Marini, A. Nigro, M. Raso

*Dipartimento di Fisica, Univ. 'La Sapienza' and INFN, Rome, Italy* <sup>f</sup>

C. Cormack, J.C. Hart, N.A. McCubbin, T.P. Shah

*Rutherford Appleton Laboratory, Chilton, Didcot, Oxon, U.K.* <sup>o</sup>

D. Epperson, C. Heusch, H.F.-W. Sadrozinski, A. Seiden, R. Wichmann, D.C. Williams  
*University of California, Santa Cruz, CA, USA* <sup>p</sup>

N. Pavel

*Fachbereich Physik der Universität-Gesamthochschule Siegen, Germany* <sup>c</sup>

H. Abramowicz<sup>41</sup>, S. Dagan<sup>42</sup>, S. Kananov<sup>42</sup>, A. Kreisel, A. Levy<sup>42</sup>, A. Schechter

*Raymond and Beverly Sackler Faculty of Exact Sciences, School of Physics, Tel-Aviv University, Tel-Aviv, Israel* <sup>e</sup>

T. Abe, T. Fusayasu, M. Inuzuka, K. Nagano, K. Umemori, T. Yamashita

*Department of Physics, University of Tokyo, Tokyo, Japan* <sup>g</sup>

R. Hamatsu, T. Hirose, K. Homma<sup>43</sup>, S. Kitamura<sup>44</sup>, T. Nishimura

*Tokyo Metropolitan University, Dept. of Physics, Tokyo, Japan* <sup>g</sup>

M. Arneodo<sup>45</sup>, R. Cirio, M. Costa, M.I. Ferrero, S. Maselli, V. Monaco, C. Peroni, M.C. Petrucci, M. Ruspa, A. Solano, A. Staiano

*Università di Torino, Dipartimento di Fisica Sperimentale and INFN, Torino, Italy* <sup>f</sup>

M. Dardo

*II Faculty of Sciences, Torino University and INFN - Alessandria, Italy* <sup>f</sup>

D.C. Bailey, C.-P. Fagerstroem, R. Galea, T. Koop, G.M. Levman, J.F. Martin,

R.S. Orr, S. Polenz, A. Sabetfakhri, D. Simmons

*University of Toronto, Dept. of Physics, Toronto, Ont., Canada* <sup>a</sup>

J.M. Butterworth, C.D. Catterall, M.E. Hayes, E.A. Heaphy, T.W. Jones, J.B. Lane

*University College London, Physics and Astronomy Dept., London, U.K.* <sup>o</sup>

J. Ciborowski, G. Grzelak<sup>46</sup>, R.J. Nowak, J.M. Pawlak, R. Pawlak, B. Smalska,

T. Tymieniecka, A.K. Wróblewski, J.A. Zakrzewski, A.F. Żarnecki

*Warsaw University, Institute of Experimental Physics, Warsaw, Poland* <sup>j</sup>

M. Adamus, T. Gadaj

*Institute for Nuclear Studies, Warsaw, Poland* <sup>j</sup>

O. Deppe, Y. Eisenberg<sup>42</sup>, D. Hochman, U. Karshon<sup>42</sup>

*Weizmann Institute, Department of Particle Physics, Rehovot, Israel* <sup>d</sup>

W.F. Badgett, D. Chapin, R. Cross, C. Foudas, S. Mattingly, D.D. Reeder, W.H. Smith,  
A. Vaiciulis<sup>47</sup>, T. Wildschek, M. Wodarczyk

*University of Wisconsin, Dept. of Physics, Madison, WI, USA* <sup>p</sup>

A. Deshpande, S. Dhawan, V.W. Hughes

*Yale University, Department of Physics, New Haven, CT, USA* <sup>p</sup>

S. Bhadra, W.R. Friskin, R. Hall-Wilton, M. Khakzad, S. Menary, W.B. Schmidke

*York University, Dept. of Physics, Toronto, Ont., Canada* <sup>a</sup>

- <sup>1</sup> now visiting scientist at DESY
- <sup>2</sup> also at IROE Florence, Italy
- <sup>3</sup> now at Univ. of Salerno and INFN Napoli, Italy
- <sup>4</sup> also at DESY
- <sup>5</sup> supported by Worldlab, Lausanne, Switzerland
- <sup>6</sup> now a self-employed consultant
- <sup>7</sup> now at Spectral Design GmbH, Bremen
- <sup>8</sup> now at EDS Electronic Data Systems GmbH, Troisdorf, Germany
- <sup>9</sup> also at University of Hamburg, Alexander von Humboldt Research Award
- <sup>10</sup> now at Dongshin University, Naju, Korea
- <sup>11</sup> now at NASA Goddard Space Flight Center, Greenbelt, MD 20771, USA
- <sup>12</sup> now at Greenway Trading LLC
- <sup>13</sup> supported by the Polish State Committee for Scientific Research, grant No. 2P03B14912
- <sup>14</sup> now at Massachusetts Institute of Technology, Cambridge, MA, USA
- <sup>15</sup> visitor from Florida State University
- <sup>16</sup> now at Fermilab, Batavia, IL, USA
- <sup>17</sup> now at ATM, Warsaw, Poland
- <sup>18</sup> now at CERN
- <sup>19</sup> now at ESG, Munich
- <sup>20</sup> now an independent researcher in computing
- <sup>21</sup> now at University of Edinburgh, Edinburgh, U.K.
- <sup>22</sup> PPARC Advanced fellow
- <sup>23</sup> visitor of Univ. of Crete, Greece, partially supported by DAAD, Bonn - Kz. A/98/16764
- <sup>24</sup> on leave from MSU, supported by the GIF, contract I-0444-176.07/95
- <sup>25</sup> supported by DAAD, Bonn - Kz. A/98/12712
- <sup>26</sup> supported by an EC fellowship
- <sup>27</sup> PPARC Post-doctoral fellow
- <sup>28</sup> now at Osaka Univ., Osaka, Japan
- <sup>29</sup> also at University of Tokyo
- <sup>30</sup> now at Wayne State University, Detroit
- <sup>31</sup> supported by an EC fellowship number ERBFMBICT 972523
- <sup>32</sup> now at HERA-B/DESY supported by an EC fellowship No.ERBFMBICT 982981
- <sup>33</sup> supported by the Comunidad Autonoma de Madrid

<sup>34</sup> now at debis Systemhaus, Bonn, Germany

<sup>35</sup> now at Loma Linda University, Loma Linda, CA, USA

<sup>36</sup> partially supported by the Foundation for German-Russian Collaboration DFG-RFBR (grant no. 436 RUS 113/248/3 and no. 436 RUS 113/248/2)

<sup>37</sup> now at University of Florida, Gainesville, FL, USA

<sup>38</sup> supported by the Feodor Lynen Program of the Alexander von Humboldt foundation

<sup>39</sup> now with Physics World, Dirac House, Bristol, U.K.

<sup>40</sup> partly supported by Tel Aviv University

<sup>41</sup> an Alexander von Humboldt Fellow at University of Hamburg

<sup>42</sup> supported by a MINERVA Fellowship

<sup>43</sup> now at ICEPP, Univ. of Tokyo, Tokyo, Japan

<sup>44</sup> present address: Tokyo Metropolitan University of Health Sciences, Tokyo 116-8551, Japan

<sup>45</sup> now also at Università del Piemonte Orientale, I-28100 Novara, Italy, and Alexander von Humboldt fellow at the University of Hamburg

<sup>46</sup> supported by the Polish State Committee for Scientific Research, grant No. 2P03B09308

<sup>47</sup> now at University of Rochester, Rochester, NY, USA

- <sup>a</sup> supported by the Natural Sciences and Engineering Research Council of Canada (NSERC)
- <sup>b</sup> supported by the FCAR of Québec, Canada
- <sup>c</sup> supported by the German Federal Ministry for Education and Science, Research and Technology (BMBF), under contract numbers 057BN19P, 057FR19P, 057HH19P, 057HH29P, 057SI75I
- <sup>d</sup> supported by the MINERVA Gesellschaft für Forschung GmbH, the German Israeli Foundation, and by the Israel Ministry of Science
- <sup>e</sup> supported by the German-Israeli Foundation, the Israel Science Foundation, the U.S.-Israel Binational Science Foundation, and by the Israel Ministry of Science
- <sup>f</sup> supported by the Italian National Institute for Nuclear Physics (INFN)
- <sup>g</sup> supported by the Japanese Ministry of Education, Science and Culture (the Monbusho) and its grants for Scientific Research
- <sup>h</sup> supported by the Korean Ministry of Education and Korea Science and Engineering Foundation
- <sup>i</sup> supported by the Netherlands Foundation for Research on Matter (FOM)
- <sup>j</sup> supported by the Polish State Committee for Scientific Research, grant No. 115/E-343/SPUB/P03/154/98, 2P03B03216, 2P03B04616, 2P03B10412, 2P03B05315, and by the German Federal Ministry of Education and Science, Research and Technology (BMBF)
- <sup>k</sup> supported by the Polish State Committee for Scientific Research (grant No. 2P03B08614 and 2P03B06116)
- <sup>l</sup> partially supported by the German Federal Ministry for Education and Science, Research and Technology (BMBF)
- <sup>m</sup> supported by the Fund for Fundamental Research of Russian Ministry for Science and Education and by the German Federal Ministry for Education and Science, Research and Technology (BMBF)
- <sup>n</sup> supported by the Spanish Ministry of Education and Science through funds provided by CICYT
- <sup>o</sup> supported by the Particle Physics and Astronomy Research Council
- <sup>p</sup> supported by the US Department of Energy
- <sup>q</sup> supported by the US National Science Foundation

# 1 Introduction

The HERA  $ep$  collider has extended the kinematic range available for the study of deep inelastic scattering (DIS) by two orders of magnitude to values of  $Q^2$  up to about  $50000 \text{ GeV}^2$ , where  $Q^2$  is the negative square of the four-momentum transfer between the lepton and proton. Measurements in this domain allow new searches for physics processes beyond the Standard Model (SM) at characteristic mass scales in the TeV range. A wide class of such hypothesized new interactions would modify the differential DIS cross sections in a way which can be parameterized by effective four-fermion contact interactions (CI) which couple electrons to quarks. This analysis was stimulated in part by an excess of events over the SM expectation for  $Q^2 \gtrsim 20000 \text{ GeV}^2$  reported recently by the ZEUS [1] and H1 [2] collaborations, for which CI scenarios have been suggested as possible explanations (see e.g. [3–6]).

In a recent publication [7], the Born cross sections at  $Q^2 > 400 \text{ GeV}^2$  extracted from  $47.7 \text{ pb}^{-1}$  of ZEUS neutral-current (NC)  $e^+p$  DIS data collected during the years 1994–1997 have been compared to the SM predictions primarily derived from measurements at lower  $Q^2$ , extrapolated to the HERA kinematic regime. The agreement is generally good. The only discrepancy is due to the high- $Q^2$  excess of events in the data taken before 1997, which has not been corroborated by the 1997 data but is still present in the combined sample with reduced significance. The present paper presents a comparison of the full data sample to SM predictions modified by various hypothetical  $eeqq$  CI scenarios. Limits on the CI strength and on the effective mass scale  $\Lambda$  are determined for the different CI types.

Limits on  $eeqq$  CI parameters have been reported previously by the H1 collaboration [8], by the LEP collaborations (ALEPH [9], DELPHI [10], L3 [11, 12], OPAL [13]), and by the Tevatron experiments CDF [14] and DØ [15].

This paper is organized as follows: after a synopsis of the relevant theoretical aspects in Sect. 2, the experimental setup, the event selection and reconstruction procedures, and the Monte Carlo (MC) simulation are discussed in Sect. 3. The CI analysis methods are presented in Sect. 4, and the results are summarized in Sect. 5. A discussion of the statistical issues related to the limit setting and the information needed to combine the results of this analysis with those of other experiments are given in the Appendix.

## 2 Contact–Interaction Scenarios

A broad range of hypothesized non-SM processes at mass scales beyond the HERA center-of-mass energy,  $\sqrt{s} = 300 \text{ GeV}$ , can be approximated in their low-energy limit by  $eeqq$

contact interactions (Fig. 1), analogous to the effective four–fermion interaction describing the weak force at low energies [16]. Examples include the exchange of heavy objects with mass  $M \gg \sqrt{s}$  such as leptoquarks or vector bosons [17] and the exchange of common constituents between the lepton and quark in compositeness models [18, 19]. Note that the CI approach is an effective theory which is not renormalizable and is only asymptotically valid in the low–energy limit.

In the presence of  $eeqq$  CIs which couple to a specific quark flavor ( $q$ ), the SM Lagrangian  $\mathcal{L}_{\text{SM}}$  receives the following additional terms [17–20]:

$$\begin{aligned} \mathcal{L} = \mathcal{L}_{\text{SM}} + \epsilon \frac{g^2}{\Lambda^2} & \left[ \eta_s^q (\bar{e}_L e_R) (\bar{q}_L q_R) + \eta_{s'}^q (\bar{e}_L e_R) (\bar{q}_R q_L) + \text{h.c.} \right. & \text{scalar} \\ & + \eta_{LL}^q (\bar{e}_L \gamma^\mu e_L) (\bar{q}_L \gamma_\mu q_L) + \eta_{LR}^q (\bar{e}_L \gamma^\mu e_L) (\bar{q}_R \gamma_\mu q_R) & (1) \\ & + \eta_{RL}^q (\bar{e}_R \gamma^\mu e_R) (\bar{q}_L \gamma_\mu q_L) + \eta_{RR}^q (\bar{e}_R \gamma^\mu e_R) (\bar{q}_R \gamma_\mu q_R) & \text{vector} \\ & \left. + \eta_T^q (\bar{e}_L \sigma^{\mu\nu} e_R) (\bar{q}_L \sigma_{\mu\nu} q_R) + \text{h.c.} \right], & \text{tensor} \end{aligned}$$

where the subscripts  $L$  and  $R$  denote the left– and right–handed helicity projections of the fermion fields,  $g$  is the overall coupling, and  $\Lambda$  is the effective mass scale. Since  $g$  and  $\Lambda$  always enter in the combination  $g^2/\Lambda^2$ , we adopt the convention  $g^2 = 4\pi$  so that CI strengths are determined by the effective mass scale,  $\Lambda$ . The overall sign of the CI Lagrangian is denoted by  $\epsilon$  in eq. (1). Note that  $\epsilon = +1$  and  $\epsilon = -1$  represent separate CI scenarios which are related to different underlying physics processes. The  $\eta$  coefficients determine the relative size and sign of the individual terms. Only the vector terms are considered in this study since strong limits beyond the HERA sensitivity have already been placed on the scalar and tensor terms (see [3, 5, 17] and references therein). In the following, only CI scenarios will be discussed for which each of the  $\eta_{mn}^q$  ( $m, n = L, R$ ) is either zero or  $\pm 1$ .

The relevant kinematic variables for this analysis are  $Q^2$ ,  $x$  and  $y$ , which are defined in the usual way in terms of the four–momenta of the incoming positron ( $k$ ), the incoming proton ( $P$ ), and the scattered positron ( $k'$ ) as  $Q^2 = -q^2 = -(k - k')^2$ ,  $x = Q^2/(2q \cdot P)$ , and  $y = (q \cdot P)/(k \cdot P)$ . The leading–order, neutral–current  $ep$  SM cross section is given by

$$\frac{d^2\sigma^{\text{NC}}(e^\pm p)}{dx dQ^2}(x, Q^2) = \frac{2\pi\alpha^2}{xQ^4} \left[ (1 + (1 - y)^2) F_2^{\text{NC}} \mp (1 - (1 - y)^2) xF_3^{\text{NC}} \right], \quad (2)$$

$$F_2^{\text{NC}}(x, Q^2) = \sum_{q=d,u,s,c,b} A_q(Q^2) \cdot [xq(x, Q^2) + x\bar{q}(x, Q^2)], \quad (3)$$

$$xF_3^{\text{NC}}(x, Q^2) = \sum_{q=d,u,s,c,b} B_q(Q^2) \cdot [xq(x, Q^2) - x\bar{q}(x, Q^2)], \quad (4)$$

where  $q(x, Q^2)$  and  $\bar{q}(x, Q^2)$  are the parton distribution functions for quarks and anti-

quarks,  $\alpha$  is the fine structure constant, and  $A_q$  and  $B_q$  are defined as follows:

$$\begin{aligned} A_q(Q^2) &= \frac{1}{2} [(V_q^L)^2 + (V_q^R)^2 + (A_q^L)^2 + (A_q^R)^2] , \\ B_q(Q^2) &= [(V_q^L)(A_q^L) - (V_q^R)(A_q^R)] . \end{aligned} \quad (5)$$

Terms resulting from CIs can be included in eqs. (2-5) by replacing the SM coefficient functions  $V_q^{L,R}$  and  $A_q^{L,R}$  with

$$\begin{aligned} V_q^m &= Q_q - (v_e \pm a_e) v_q \chi_Z + \frac{\epsilon Q^2}{2\alpha\Lambda^2} (\eta_{mL}^q + \eta_{mR}^q) , \\ A_q^m &= - (v_e \pm a_e) a_q \chi_Z + \frac{\epsilon Q^2}{2\alpha\Lambda^2} (\eta_{mL}^q - \eta_{mR}^q) , \\ v_f &= T_f^3 - 2 \sin^2 \theta_W Q_f , \\ a_f &= T_f^3 , \\ \chi_Z &= \frac{1}{4 \sin^2 \theta_W \cos^2 \theta_W} \frac{Q^2}{Q^2 + M_Z^2} . \end{aligned} \quad (6)$$

In eq. (6), the subscript  $m$  is  $L$  or  $R$ ; the plus (minus) sign in the definitions of  $V_q^m$  and  $A_q^m$  is for  $m = L$  ( $m = R$ ). The coefficients  $v_f$  and  $a_f$  are the SM vector and axial-vector coupling constants of an electron ( $f = e$ ) or quark ( $f = q$ );  $Q_f$  and  $T_f^3$  denote the fermion's charge and third component of the weak isospin;  $M_Z$  and  $\theta_W$  are the  $Z$  mass and the Weinberg angle. In the limit  $\Lambda \rightarrow \infty$ , the coefficient functions  $V_q^m$  and  $A_q^m$  in eq. (6) reduce to their SM forms.

As can be seen from eqs. (2-6), the effect of a CI on the NC DIS cross section depends on the specific scenario. In general, two kinds of additional terms are produced. One kind is proportional to  $1/\Lambda^4$  and enhances the cross section at high  $Q^2$ . The second is proportional to  $1/\Lambda^2$  and is caused by interference with the SM amplitude, which can either enhance or suppress the cross section at intermediate  $Q^2$ . The predicted ratio (SM+CI)/SM of  $d^2\sigma/(dQ^2 dx)$  depends on  $Q^2$  at fixed  $x$ , but also on  $x$  at fixed  $Q^2$  due to the different  $y$  dependences of the coefficient functions multiplying the  $F_2$  and  $F_3$  terms in eq. (2). Note that CIs induce modifications of the SM cross section for all  $x$  and  $Q^2$ , in contrast e.g. to the direct production of an  $eq$  resonance in the  $s$ -channel.

For  $ep$  scattering at HERA, the contribution of second- and third-generation quarks to CI cross-section modifications is suppressed by the respective parton distribution functions in the proton. For the present analysis, flavor symmetry,

$$\eta_{mn}^d = \eta_{mn}^s = \eta_{mn}^b \quad \text{and} \quad \eta_{mn}^u = \eta_{mn}^c \quad (7)$$

is assumed unless explicitly stated otherwise. The CI limits reported here are only weakly

sensitive to this assumption.<sup>1</sup> Contributions from the top quark content of the proton are almost completely suppressed due to the large top mass and are neglected in this analysis.

Using the relations in eq. (7), there are eight independent vector terms in eq. (1), which lead to a large list of possible CI scenarios. To reduce this list, we consider the following:

- Recent measurements of parity-violating transition amplitudes in cesium atoms [21] imply very restrictive constraints on CIs [5, 22, 23]. These limits are avoided by parity-conserving CI scenarios, i.e. if

$$\eta_{LL}^q + \eta_{LR}^q - \eta_{RL}^q - \eta_{RR}^q = 0 . \quad (8)$$

Conforming to this constraint, in particular, excludes CIs of purely chiral type, i.e. those for which the  $\eta_{mn}^q$  are non-zero only for one combination of  $m$  and  $n$ .

- $SU(2)_L$  invariance requires  $\eta_{RL}^u = \eta_{RL}^d$  [5]. Terms violating this relation are considered only for  $u$  quarks, which dominate the high- $x$  cross section at HERA, and hence show the largest CI-SM interference effects for a given  $\Lambda$ . A CI signal from this source could therefore manifest itself in  $ep$  collisions while avoiding strong  $SU(2)$ -breaking effects e.g. at LEP.

Based on these considerations, the 30 specific CI scenarios listed in Table 1 are explored in this paper. Note that each line in this table represents two scenarios, one for  $\epsilon = +1$  and one for  $\epsilon = -1$  (denoted as  $VV^+$ ,  $VV^-$  etc.). All scenarios respect eq. (8), and all scenarios except U2, U4 and U6 obey  $SU(2)$  symmetry. The  $SU(2)$ -conserving CI scenarios with  $\eta_{LL}^u \neq \eta_{LL}^d$  (U1 and U3) would also induce an  $e\nu qq$  CI signal in charged-current (CC) DIS,  $e^+p \rightarrow \bar{\nu}X$ . We have not used the CC data sample to constrain further these scenarios.

Several examples of modifications of the SM cross sections by CIs are illustrated in Fig. 2. The cross-section modifications for the X1–X6 and the corresponding U1–U6 scenarios are similar, demonstrating that the  $d$  quarks have little impact on the CI analysis.

### 3 Experimental Setup and Data Samples

This analysis uses the data samples, Monte Carlo simulation, event selection, kinematic reconstruction, and assessment of systematic effects used in the NC DIS analysis described in [7]. The data were collected during the years 1994–1997 in  $e^+p$  collisions with beam energies  $E_e = 27.5$  GeV and  $E_p = 820$  GeV. The relevant aspects of the experimental

---

<sup>1</sup> A similar statement is true for the Tevatron CI limits from lepton-pair production, which also depend on the parton distributions in the proton. In contrast, the CI analyses at LEP are sensitive to the cross section  $\sigma(e^+e^- \rightarrow \text{hadrons})$  and the resulting limits depend strongly on flavor symmetry assumptions.

setup, event selection, and reconstruction are summarized briefly below. More details can be found in [7].

The ZEUS detector is described in detail elsewhere [24]. The main components used in the present analysis are the central tracking detector (CTD) [25], positioned in a 1.43 T solenoidal magnetic field, and the compensating uranium–scintillator sampling calorimeter (CAL) [26], subdivided into forward (FCAL), barrel (BCAL) and rear (RCAL) sections. Under test beam conditions, the CAL energy resolution is  $\sigma(E)/E = 18\%/\sqrt{E \text{[GeV]}}$  for electrons and  $35\%/\sqrt{E \text{[GeV]}}$  for hadrons. A three-level trigger is used to select events online. The trigger decision is based mainly on energies deposited in the calorimeter, specifically on the electromagnetic energy, on the total transverse energy, and on<sup>2</sup>  $E - p_Z = \sum_i E_i (1 - \cos \theta_i)$  (the sum running over all calorimeter energy deposits). For fully contained events, the expected value of  $E - p_Z$  is given by  $2E_e = 55 \text{ GeV}$ . Timing cuts are used to reject beam–gas interactions and cosmic rays.

The luminosity is measured to a precision of 1.6% from the rate of energetic bremsstrahlung photons produced in the process  $ep \rightarrow ep\gamma$  [27].

The offline event reconstruction applies an algorithm to identify the scattered positron using the topology of its calorimeter signal and the tracking information. The measured energies are corrected for energy loss in inactive material between the interaction point and the calorimeter, for calorimeter inhomogeneities, and for effects caused by redirected hadronic energy from interactions in material between the primary vertex and the calorimeter or by backsplash from the calorimeter (albedo). The kinematic variables for NC DIS candidate events are calculated from the scattering angle of the positron and from an angle representing the direction of the scattered quark. The latter is determined from the transverse momentum and the  $E - p_Z$  of all energy deposits except those assigned to the scattered positron.

The appropriately corrected experimental quantities are used to make the offline event selection. The major criteria are [7]: (i) the event vertex must be reconstructed from the tracking information, with  $|Z_{\text{vtx}}| < 50 \text{ cm}$ ; (ii) an isolated scattered positron with energy  $E'_e > 10 \text{ GeV}$  has to be identified; (iii)  $38 \text{ GeV} < E - p_Z < 65 \text{ GeV}$ ; (iv)  $y_e < 0.95$ , where  $y_e$  is the value of  $y$  as reconstructed from the measured energy and angle of the scattered  $e^+$ . The requirements (iii) and (iv) reject background events from photoproduction.

Monte Carlo simulations are used to model the expected distributions of the kinematic variables  $x$ ,  $y$  and  $Q^2$  and to estimate the rate of photoproduction background events. NC DIS events including radiative effects are simulated using the HERACLES 4.5.2 [28]

---

<sup>2</sup> ZEUS uses a right-handed Cartesian coordinate system centered at the nominal interaction point, with the  $Z$  axis pointing in the proton beam direction. The polar angle is defined with respect to this system in the usual way.

program with the DJANGO 6.24 [29] interface to the hadronization programs. In HERACLES, corrections for initial– and final–state radiation, vertex and propagator corrections, and two–boson exchange are included. The underlying cross sections are calculated in next–to–leading order QCD using the CTEQ4D parton distribution set [30]. The NC DIS hadronic final state is simulated using the color–dipole model of ARIADNE 4.08 [31] and, as a systematic check, the MEPS option of LEPTO 6.5 [32] for the QCD cascade. Both programs use the Lund string model of JETSET 7.4 [33] for the hadronization. MC samples of photoproduction background events are produced using the HERWIG 5.8 [34] generator. All MC signal and background events are passed through the detector simulation based on GEANT [35], incorporating the effects of the trigger. They are subsequently processed with the same reconstruction and analysis programs used for the data. All MC events are weighted to represent the same integrated luminosity as the experimental data.

Good agreement is found in [7] both between the distributions of kinematic variables in data and MC, and between the measured differential cross sections  $d\sigma/dQ^2$ ,  $d\sigma/dx$  and  $d\sigma/dy$  and the respective SM predictions, with the possible exception of the two events at  $Q^2 > 35000 \text{ GeV}^2$ .

## 4 Analysis Method

The CI analysis compares the distributions of the measured kinematic variables with the corresponding distributions from a MC simulation of events of the type  $e^+p \rightarrow e^+X$ , with the weight

$$w = \left. \frac{\frac{d^2\sigma}{dx dQ^2}(\text{SM+CI})}{\frac{d^2\sigma}{dx dQ^2}(\text{SM})} \right|_{\text{true } x,y,Q^2} \quad (9)$$

applied to each reconstructed MC event in order to simulate the CI scenarios. For the calculation of  $w$ , leading–order cross sections are employed with the “true” values of  $x$ ,  $y$  and  $Q^2$  determined from the four–momentum of the exchanged boson and the beam momenta. In cases where a photon with energy  $E_\gamma$  is radiated off the incoming positron (initial state radiation), the  $e$  beam energy is reduced by the energy of the radiated photon. The reweighting procedure using eq. (9) accounts correctly for correlations between the effects of a CI signal and the pattern of acceptance losses and migrations.

The simulated background events from photoproduction are added to the selected NC–DIS MC data sets. The photoproduction contamination is highest at high  $y$  and is estimated to be less than 0.5% overall and below 3% in any of the bins used for the cross–section measurements in [7].

For each of the CI scenarios, two statistical methods are used. Each incorporates a log-likelihood function

$$L(\epsilon/\Lambda^2) = - \sum_{i \in \text{data}} \log p_i(\epsilon/\Lambda^2) , \quad (10)$$

where the  $p_i$  are appropriately normalized probabilities which are derived from a comparison of measured and simulated event distributions ( $i$  runs over individual events in method 1 and over bins of a histogram in method 2, see below). Note that the two CI scenarios corresponding to two sets of  $\eta_{mn}^q$  values differing only in the overall sign  $\epsilon$  are combined into one log-likelihood function. A description of the data samples used for evaluating  $L(\epsilon/\Lambda^2)$  is given in Table 2 for both methods.

- Unbinned fit to the  $(x, y)$ -distribution:

In the first method, an unbinned log-likelihood technique is used to calculate  $L_1(\epsilon/\Lambda^2)$  from the individual kinematic event coordinates  $(x_i, y_i)$ . The sum in eq. (10) runs over all events in the selected data sample. The MC events are appropriately reweighted to simulate a CI scenario with strength  $\epsilon/\Lambda^2$ , as outlined in eq. (9). The probability density  $p(x, y; \epsilon/\Lambda^2)$  required to calculate  $p_i(\epsilon/\Lambda^2) = p(x_i, y_i; \epsilon/\Lambda^2)$  is determined from the resulting density of MC events in  $x$  and  $y$ . Since  $p(x, y; \epsilon/\Lambda^2)$  is normalized to unity,  $L_1$  tests the shape of the  $(x, y)$ -distribution but is independent of its absolute normalization<sup>3</sup>.

The sensitivity of the results to systematic effects is studied by repeating the limit setting procedure (see below) for analysis parameters and selection requirements which are varied within admissible ranges. These systematic checks include those which were performed in the underlying cross-section analysis [7]:

- use of MC samples generated with the MEPS instead of the ARIADNE option (as described in Sect. 3);
- use of MC samples generated with the parton distribution set MRSA [36] instead of CTEQ4D;
- variations of trigger or reconstruction efficiencies and of experimental resolutions within their uncertainties by suitably reweighting the MC events;
- modifications of the cuts and parameters used for event reconstruction and selection;
- variation of the calorimeter energy scales in the analysis of the data but not in that of the MC events.

---

<sup>3</sup> A discussion of a probabilistic interpretation of the log-likelihood function based on a Bayesian approach can be found in the Appendix.

In addition, systematic uncertainties related to the CI fitting procedure are investigated by

- changing the amount of photoproduction background in the MC sample by  $\pm 100\%$ ;
- modifying details of the method used to infer  $p(x, y; \epsilon/\Lambda^2)$  from the MC event distributions;
- calculating the CI cross sections in the following alternative ways:
  - with different parton distribution functions,
  - using NLO instead of LO QCD calculations and parton distributions,
  - with the couplings restricted to first-generation quarks ( $\eta_{mn}^s = \eta_{mn}^b = \eta_{mn}^c = 0$ ),
  - with the couplings restricted to first- and second-generation quarks ( $\eta_{mn}^b = 0$ ).

The procedure to determine limits on the CI parameters including the information from the systematic checks is discussed at the end of this section.

- Binned fit to the  $Q^2$  distribution:

In the second method,  $L_2(\epsilon/\Lambda^2)$  is determined from the  $Q^2$  distributions, using Poisson statistics for the numbers of events in each  $Q^2$  interval. Here, the sum in eq. (10) runs over all  $Q^2$  bins.  $L_2$  is sensitive to both the shape and the absolute normalization of the  $Q^2$  distribution.

The systematic uncertainties are included in  $L_2$  using the assumptions that they are fully correlated between bins and that the probability densities for all uncertainties have Gaussian shapes. The effects taken into account are equivalent to those described above for the unbinned method and include in addition a 1.6% uncertainty on the integrated luminosity.

It has been demonstrated that both methods provide unbiased estimates of the CI strength when applied to MC samples. The resulting log-likelihood functions  $L_1$  and  $L_2$  agree with each other for most of the CI scenarios under study. However, for a few scenarios such as X2<sup>−</sup> and X3<sup>−</sup>,  $L_1$  rises faster than  $L_2$  with decreasing  $\Lambda$ . This can be understood as a consequence of the fact that  $L_1$  uses the full two-dimensional information of the  $(x, y)$  distribution and is hence more sensitive to those scenarios which imply a marked  $x$ -dependence of the cross-section modification at fixed  $Q^2$ . A few examples of comparisons of  $L_1$  with  $L_2$  are shown in Fig. 3.

The best estimates,  $\Lambda_0$ , for the different CI scenarios are given by the positions of the respective minima of  $L_{1,2}(\epsilon/\Lambda^2)$  with  $\epsilon = -1$  and  $\epsilon = +1$ . The values of  $\epsilon/\Lambda_0^2$  resulting from the unbinned method are indicated in Fig. 4. Note that  $1/\Lambda_0^2 = 0$  is taken for all cases where  $L_{1,2}(\epsilon/\Lambda^2)$  rises monotonically for a given scenario, i.e. for  $\epsilon = +1$  or  $\epsilon = -1$  (see Fig. 3).

For calculating confidence intervals (i.e. limits) of  $\epsilon/\Lambda^2$ , one usually employs an analysis of the log-likelihood functions  $L(\epsilon/\Lambda^2)$  (referred to as the “ $L$ –analysis” in the following). A discussion of some aspects related to the  $L$ –analysis approach can be found in the Appendix, where we also provide polynomial parameterizations for  $L_1(\epsilon/\Lambda^2)$ , which may prove useful for combining our results with those from other experiments. One problem with the  $L$ –analysis is that its results depend on the choice of the “canonical variable” in terms of which it is performed; for example the  $\Lambda$  limits are different if  $L$  is evaluated as a function of  $\epsilon/\Lambda$  instead of  $\epsilon/\Lambda^2$ . In order to avoid this ambiguity, we have used MC experiments (MCE), i.e. statistically independent MC data samples corresponding to the data luminosity. For a given CI scenario, the lower limit of  $\Lambda$  at 95% C.L. was calculated by determining the value of  $\Lambda$  at which 95% of such MCEs produce most likely values of  $|\epsilon/\Lambda^2|$  larger than that found in the data. In the cases where  $1/\Lambda_0^2 \neq 0$ , the MCEs are also used to estimate the probability  $p_{\text{SM}}$  that a statistical fluctuation in an experiment with the SM cross section would produce a value of  $\Lambda_0$  smaller than that obtained from the data. Note that a high value of  $p_{\text{SM}}$  does not in itself signify that the SM prediction describes the data well, but indicates that the inclusion of the CI scenario under study does not significantly improve the agreement between data and prediction.

For the two–dimensional fitting method, the above procedure is performed for each systematic check. The resulting CI limits are scattered around the limits of the central analysis, with deviations in both directions being about equally frequent. The  $\Lambda$  limits deviate from their central values by typically less than 15%, though by as much as 30% in a few cases. The overall limits including systematic effects are finally extracted by combining the MCE sets of all systematic checks and applying the limit setting procedure described above to this overall MCE sample. This corresponds to assigning equal *a priori* probabilities to each of the tested variations and reflects the fact that by construction we cannot exclude or favor any of them.

The  $\Lambda$  limits resulting from both methods agree to within 15% in all cases except for the scenarios  $\text{AA}^+$ ,  $\text{X2}^-$  and  $\text{X3}^-$ , for which the two–dimensional method has higher sensitivity and correspondingly yields significantly stronger limits. Therefore, the results of this method are presented in the following.

## 5 Results

The resulting SM probabilities  $p_{\text{SM}}$  (see Table 3) do not indicate significant amplitudes for any of the CI scenarios considered. Therefore, we report upper limits on  $1/\Lambda^2$  and the corresponding lower limits on  $\Lambda$ .

A selection of plots demonstrating the expected modifications of the  $Q^2$ – and  $x$ –distri-

butions in the presence of CIs with strengths corresponding to the 95% C.L. exclusion limits is shown in Figs. 5 and 6.<sup>4</sup> As mentioned in Sect. 1, the data show an excess over the SM predictions at  $Q^2 \gtrsim 35000 \text{ GeV}^2$ . However, it is apparent that CIs cannot provide an improved description of this excess while simultaneously describing the data well at lower  $Q^2$ , where data and SM expectation are in good agreement. These figures also confirm that the  $x$ -dependence of the (SM+CI)/SM cross-section ratio differs markedly between different CI scenarios and obviously contributes to the sensitivity of the CI fit, e.g. in the X3 case. This statement is generally true for all cases where the limits derived from the two analysis methods differ significantly.

The lower limits on  $\Lambda$  ( $\Lambda_{\text{lim}}^\pm$ ) and the probabilities  $p_{\text{SM}}$  are summarized in Table 3 and are displayed in Fig. 4. In none of the cases does the SM probability fall below 16%. The  $\Lambda$  limits range from 1.7 TeV to 5 TeV. Those few cases with limits below 2.5 TeV correspond to log-likelihood functions having a broad minimum, either in the region with  $\epsilon = +1$  (X1, U1) or with  $\epsilon = -1$  (X6, U6); these minima correspond to parameter combinations for which the pure CI×CI contribution and the CI×SM interference term approximately cancel in the HERA kinematic regime.<sup>5</sup>

Table 4 shows a comparison of the ZEUS CI results with corresponding limits reported recently by other experiments which study  $eeqq$  CIs in  $e^+e^-$  scattering at LEP (ALEPH [9], L3 [12], OPAL [13]) or via Drell–Yan pair production in  $p\bar{p}$  scattering (CDF [14], DØ [15]). The H1 [8] and DELPHI [10] collaborations report results only for purely chiral CIs which cannot be compared to the results of this paper. All limits shown in Table 4 have been derived assuming flavor symmetry (see eq. (7)), except the LEP limits for the U3 and U4 scenarios which are for first-generation quarks only. Limits for the X2, X5, U1, U2, U5 and U6 scenarios are not included in Table 4 because there exist no previously published results. ZEUS and the other experiments are all sensitive to CIs at mass scales of a few TeV. The relative sensitivity to different CI scenarios depends on the CI×SM interference sign which is opposite in  $e^+p$  scattering on the one hand and in  $e^+e^-$  and  $p\bar{p}$  scattering on the other.<sup>6</sup> Where available, the LEP limits often exceed the results of this paper, although it should be noted that this depends on the assumption of a flavor-symmetric CI structure. Limits for CIs which couple only to first-generation quarks would differ only by a small amount from those reported here for  $ep$  or  $p\bar{p}$  scattering, but would be significantly weaker in the case of LEP.

---

<sup>4</sup> Note that the binning of the data in  $x$  and  $Q^2$  used for this presentation is irrelevant in the analysis of the limits provided in Table 3.

<sup>5</sup> Note that these cancellations happen at opposite  $\epsilon$  for  $e^-p$  scattering.

<sup>6</sup> The CI limits from CDF and the LEP experiments have been quoted here according to the sign convention used in the cited papers.

## 6 Conclusions

We have searched for indications of  $eeqq$  contact interactions in  $47.7 \text{ pb}^{-1}$  of ZEUS high- $Q^2$   $e^+p$  neutral-current deep inelastic scattering data. The distributions of the kinematic variables in the data have been compared to predictions derived for 30 scenarios of vector contact interactions which differ in their helicity structure and quark-flavor dependence. In none of the cases has a significant indication of a contact interaction been found and 95% C.L. upper limits on  $1/\Lambda^2$  have been determined for each of these scenarios. The lower limits on  $\Lambda$  range between 1.7 TeV and 5 TeV and are found to be largely independent of the statistical method applied.

The results exhibit a sensitivity to contact interactions similar to that recently reported by other experiments; in order to allow full use to be made of the available experimental data, the information needed to combine the results of this analysis with those from other sources is provided. Some of the limits reported here are the most restrictive yet published, and several of the contact-interaction scenarios have been studied in this paper for the first time.

*Acknowledgments:* We appreciate the contributions to the construction and maintenance of the ZEUS detector by many people who are not listed as authors. We especially thank the DESY computing staff for providing the data analysis environment and the HERA machine group for their outstanding operation of the collider. Finally, we thank the DESY directorate for strong support and encouragement.

This paper was completed shortly after the tragic and untimely death of Prof. Dr. B. H. Wiik, Chairman of the DESY directorate. All members of the ZEUS collaboration wish to acknowledge the remarkable rôle which he played in the success of both the HERA project and of the ZEUS experiment. His inspired scientific leadership, his warm personality and his friendship will be sorely missed by us all.

## Appendix: The Log–Likelihood Functions

In this Appendix we summarize some aspects of interpreting the log–likelihood functions  $L(\epsilon/\Lambda^2)$  using a Bayesian probabilistic approach. The results of the unbinned method described in Sect. 4 have been employed here, but systematic effects have not been taken into account. For simplicity, we will denote the log–likelihood functions by  $L$  instead of  $L_1$  in this Appendix.

For ease of calculation, the functions  $L(\epsilon/\Lambda^2) - L_{\min}$  have been parameterized as eighth–order polynomials in the region where  $L(\epsilon/\Lambda^2) - L_{\min} < 18$ , corresponding approximately to a  $\pm 6\sigma$  interval around the minimum of  $L$ . The polynomial coefficients are summarized in Table 5. The accuracy of the parameterizations is typically better than 0.1 units in  $L$ . Note that, neglecting systematic effects, these parameterizations allow one to combine the ZEUS results with those of other experiments by simply adding the  $L$  functions and repeating the analysis described below.

The Bayesian approach starts from the relation

$$p(\epsilon/\Lambda^2|\mathcal{D}) \propto p(\mathcal{D}|\epsilon/\Lambda^2) \cdot p_0(\epsilon/\Lambda^2) , \quad (11)$$

where  $\mathcal{D}$  symbolizes the experimental data,  $p(\mathcal{D}|\epsilon/\Lambda^2)$  is the conditional probability to observe  $\mathcal{D}$  for a given value of  $\epsilon/\Lambda^2$ , and  $p_0(\epsilon/\Lambda^2)$  is the *prior probability* describing the knowledge about  $\epsilon/\Lambda^2$  before the experiment was conducted. The probability  $p(\epsilon/\Lambda^2|\mathcal{D})$  assigned to  $\epsilon/\Lambda^2$  under the condition of having observed  $\mathcal{D}$  is what we actually want to derive.

In the following, we will identify

$$p(\mathcal{D}|\epsilon/\Lambda^2) \propto \exp(-L(\epsilon/\Lambda^2)) , \quad (12)$$

with the normalization appropriately fixed to unity. In the simplest case of a Gaussian probability distribution,  $L(\epsilon/\Lambda^2)$  is a parabola, and  $\sigma_{\epsilon/\Lambda^2}$ , the RMS width of  $p(\mathcal{D}|\epsilon/\Lambda^2)$ , corresponds to the width of the Gaussian. Even though some of the  $L(\epsilon/\Lambda^2)$  functions of the CI analysis are not parabola–like,  $\sigma_{\epsilon/\Lambda^2}$  is still well defined and can be interpreted as a measure of the experimental sensitivity to a given CI scenario. The values of  $\sigma_{\epsilon/\Lambda^2}$  are summarized in Table 3.

Usually, simple assumptions about  $p_0(\epsilon/\Lambda^2)$  are made in order to calculate  $p(\epsilon/\Lambda^2|\mathcal{D})$ , which only weakly depends on these assumptions provided that the width of  $p_0(\epsilon/\Lambda^2)$  is much larger than  $\sigma_{\epsilon/\Lambda^2}$ . We have calculated  $p(\epsilon/\Lambda^2|\mathcal{D})$  using a flat prior probability restricted to either  $\epsilon \geq 0$  or  $\epsilon \leq 0$ . One–sided 95% C.L. limits in the Bayesian approach

$(\Lambda_{\text{lim},B}^{\pm})$  have been determined by solving

$$\frac{\int_0^{1/(\Lambda_{\text{lim},B}^+)^2} d\xi \exp(-L(\xi))}{\int_0^{\infty} d\xi \exp(-L(\xi))} = 0.95 \quad \text{and} \quad \frac{\int_0^{-1/(\Lambda_{\text{lim},B}^-)^2} d\xi \exp(-L(\xi))}{\int_{-\infty}^0 d\xi \exp(-L(\xi))} = 0.95. \quad (13)$$

For all CI scenarios, the results deviate by less than 20% from the limits  $\Lambda_{\text{lim}}$  resulting from the MCE method (see Sect. 4). Note that systematic effects have not been considered for this cross check.

An alternative way to present the results of this search analysis is obtained by considering the ratio of two equations of the type (11) for different values of  $\epsilon/\Lambda^2$ , where one is taken as a reference value (chosen to be  $\epsilon/\Lambda^2 = 0$ , i.e. corresponding to the SM). Rearranging the terms yields

$$\frac{p(\epsilon/\Lambda^2|\mathcal{D})}{p_0(\epsilon/\Lambda^2)} \Big/ \frac{p(\epsilon/\Lambda^2 = 0|\mathcal{D})}{p_0(\epsilon/\Lambda^2 = 0)} = \frac{p(\mathcal{D}|\epsilon/\Lambda^2)}{p(\mathcal{D}|\epsilon/\Lambda^2 = 0)} = R(\epsilon/\Lambda^2), \quad (14)$$

where the double ratio on the left-hand side quantifies how the probability assigned to a given value of  $\epsilon/\Lambda^2$  changes due to the experimental data  $\mathcal{D}$ , with the reference point,  $\epsilon/\Lambda^2 = 0$ , fixing the normalization. The function  $R(\epsilon/\Lambda^2)$  has been discussed in detail elsewhere (see e.g. [37] and references therein). The representation of eq. (14) is independent of the prior probability and can be used to combine the results of this analysis with those of other experiments by analyzing the product of corresponding  $R$  functions. Note that  $R$  does not involve integrations over  $\epsilon/\Lambda^2$  and is hence invariant with respect to the variable transformations mentioned in Sect. 4; in particular,  $R$  can be interpreted both as a function of  $\epsilon/\Lambda^2$  and as a function of  $\Lambda$ . By definition,  $R$  asymptotically approaches unity if  $\epsilon/\Lambda^2 \rightarrow 0$  or  $\Lambda \rightarrow \infty$ , indicating the loss of experimental sensitivity as the CI strength vanishes. Regions where  $R$  is close to zero are excluded by  $\mathcal{D}$ , whereas  $R > 1$  indicates “signal-type” regions where the experimental data are better described by a CI scenario than by the SM. Typical  $R$  values for significant deviations from the SM are expected to exceed unity by several orders of magnitude (cf. the discussion in [37]). Two representative examples of the functions  $R(\Lambda)$  observed in the CI analysis are shown in Fig. 7. In none of the scenarios from Table 1 does  $R$  exceed unity by more than 40%, corroborating the conclusion that there is no significant indication for the presence of CIs. The threshold-type region of  $R(\Lambda)$  indicates the position of the  $\Lambda$  limit. Indeed one obtains limits similar to those reported in Sect. 5 by solving the condition  $R(\Lambda_{\text{lim},R}^{\pm}) = 0.05$  for  $\Lambda_{\text{lim},R}^{\pm}$ .

## References

- [1] ZEUS Collaboration, J. Breitweg et al., *Z. Phys. C* **74** (1997) 207.
- [2] H1 Collaboration, C. Adloff et al., *Z. Phys. C* **74** (1997) 191.
- [3] G. Altarelli et al., *Nucl. Phys. B* **506** (1997) 3.
- [4] V. Barger et al., *Phys. Lett. B* **404** (1997) 147.
- [5] V. Barger et al., *Phys. Rev. D* **57** (1998) 391.
- [6] N. Di Bartolomeo and M. Fabbrichesi, *Phys. Lett. B* **406** (1997) 237.
- [7] ZEUS Collaboration, J. Breitweg et al., Preprint DESY-99-056, DESY (1999).
- [8] H1 Collaboration, S. Aid et al., *Phys. Lett. B* **353** (1995) 578.
- [9] ALEPH Collaboration, R. Barate et al., Preprint CERN-EP/99-042, CERN (1999), hep-ex/9904011, subm. to *Eur. Phys. J.*
- [10] DELPHI Collaboration, P. Abreu et al., Preprint CERN-EP/99-05, CERN (1999), subm. to *Eur. Phys. J.*
- [11] L3 Collaboration, M. Acciarri et al., *Phys. Lett. B* **433** (1998) 163.
- [12] L3 Collaboration, submitted paper 513 to XXIX International Conference on High Energy Physics, Vancouver, July 23–29, 1998;  
D. Bourilkov, Preprint ETHZ-IPP PR-98-02, ETH Zürich (1998), hep-ex/9806027;  
D. Bourilkov, private communication.
- [13] OPAL Collaboration, G. Abbiendi et al., *Eur. Phys. J. C* **6** (1999) 1.
- [14] CDF Collaboration, F. Abe et al., *Phys. Rev. Lett.* **79** (1997) 2198.
- [15] DØ Collaboration, D. Abbott et al., Preprint FERMILAB-PUB-98-391-E, Fermilab (1998), hep-ex/9812010, subm. to *Phys. Rev. Lett.*
- [16] E. Fermi, *Z. Phys.* **88** (1934) 161;  
E. Fermi, *Nuovo Cimento* **11** (1934) 1.
- [17] P. Haberl, F. Schrempp and H. U. Martyn, in *Proc. Workshop Physics at HERA*, ed. W. Buchmüller and G. Ingelman, Hamburg, Germany, 1991, p. 1133.
- [18] E. Eichten, K. Lane and M. Peskin, *Phys. Rev. Lett.* **50** (1983) 811.
- [19] R. Rückl, *Phys. Lett.* **129 B** (1983) 363.

- [20] R. Rückl, Nucl. Phys. **B** **234** (1984) 91.
- [21] C. S. Wood et al., Science **275** (1997) 1759.
- [22] A. Deandrea, Phys. Lett. **B** **409** (1997) 277.
- [23] L. Giusti and A. Strumia, Phys. Lett. **B** **410** (1997) 229.
- [24] ZEUS Collaboration, ed. U. Holm, Status Report, 1993.
- [25] N. Harnew et al., Nucl. Instrum. Methods **A** **279** (1989) 290;  
 B. Foster et al., Nucl. Phys. **B (Proc. Suppl.)** **32** (1993) 181;  
 B. Foster et al., Nucl. Instrum. Methods **A** **338** (1994) 254.
- [26] M. Derrick et al., Nucl. Instrum. Methods **A** **309** (1991) 77;  
 ZEUS Calorimeter group, A. Andresen et al., Nucl. Instrum. Methods **A** **309** (1991) 101;  
 A. Caldwell et al., Nucl. Instrum. Methods **A** **321** (1992) 356;  
 A. Bernstein et al., Nucl. Instrum. Methods **A** **336** (1993) 23.
- [27] J. Andruszków et al., Report DESY-92-066, DESY (1992);  
 ZEUS Collaboration, M. Derrick et al., Z. Phys. **C** **63** (1994) 391.
- [28] A. Kwiatkowski, H. Spiesberger and H.-J. Möhring, Comp. Phys. Commun. **69** (1992) 155;  
 H. Spiesberger, HERACLES. *An Event Generator for ep Interactions at HERA Including Radiative Processes (Version 4.6)*, 1996, available on WWW: <http://www.desy.de/~hspiesb/heracles.html>.
- [29] K. Charchula, G. A. Schuler and H. Spiesberger, Comp. Phys. Commun. **81** (1994) 381;  
 H. Spiesberger, DJANGO6 *version 2.4 — A Monte Carlo Generator for Deep Inelastic Lepton Proton Scattering Including QED and QCD Radiative Effects*, 1996, available on WWW: <http://www.desy.de/~hspiesb/django6.html>.
- [30] CTEQ Collaboration, H. L. Lai et al., Phys. Rev. **D** **55** (1997) 1280.
- [31] L. Lönnblad, Comp. Phys. Commun. **71** (1992) 15.
- [32] G. Ingelman, A. Edin and J. Rathsman, Comp. Phys. Commun. **101** (1997) 108.
- [33] T. Sjöstrand, Comp. Phys. Commun. **39** (1986) 347;  
 T. Sjöstrand and M. Bengtsson, Comp. Phys. Commun. **43** (1987) 367;  
 T. Sjöstrand, Comp. Phys. Commun. **82** (1994) 74.
- [34] G. Marchesini et al., Comp. Phys. Commun. **67** (1992) 465.

- [35] R. Brun et al., Report CERN-DD/EE/84-1, CERN (1987).
- [36] A. D. Martin, W. J. Stirling and R. G. Roberts, Phys. Rev. **D 51** (1995) 4756.
- [37] G. D'Agostini and G. Degrassi, Preprint DFPD-99-TH-02, Univ. Padua (1999), hep-ph/9902226.

Label	$\eta_{LL}^u$	$\eta_{LR}^u$	$\eta_{RL}^u$	$\eta_{RR}^u$	$\eta_{LL}^d$	$\eta_{LR}^d$	$\eta_{RL}^d$	$\eta_{RR}^d$
VV	+1	+1	+1	+1	+1	+1	+1	+1
AA	+1	-1	-1	+1	+1	-1	-1	+1
VA	+1	-1	+1	-1	+1	-1	+1	-1
X1	+1	-1	0	0	+1	-1	0	0
X2	+1	0	+1	0	+1	0	+1	0
X3	+1	0	0	+1	+1	0	0	+1
X4	0	+1	+1	0	0	+1	+1	0
X5	0	+1	0	+1	0	+1	0	+1
X6	0	0	+1	-1	0	0	+1	-1
U1	+1	-1	0	0	0	0	0	0
U2	+1	0	+1	0	0	0	0	0
U3	+1	0	0	+1	0	0	0	0
U4	0	+1	+1	0	0	0	0	0
U5	0	+1	0	+1	0	0	0	0
U6	0	0	+1	-1	0	0	0	0

**Table 1:** The 30 scenarios for contact interactions considered in this paper. Each row of this table corresponds to two different CI scenarios for overall interference signs  $\epsilon = +1$  and  $\epsilon = -1$ , respectively (see eq. (1) in the text).

quantity	method 1	method 2
$Q_{\min}^2$ (GeV $^2$ )	500	400
$Q_{\max}^2$ (GeV $^2$ )	90200	51200
$x_{\min}$	0.04	—
$x_{\max}$	0.95	—
$y_{\min}$	0.04	—
$y_{\max}$	0.95	—
events	13243	37379

**Table 2:** The kinematic regions used for the CI analysis in the two fitting methods. Note that the cuts on  $Q^2$ ,  $x$ , and  $y$  indicated in the table are applied in addition to the event selection criteria described in Sect. 3.

CI	$\epsilon = -1$		$\epsilon = +1$		$\sigma_{\epsilon/\Lambda^2}$ $\text{TeV}^{-2}$
	$\Lambda_{\text{lim}}^-$ (TeV)	$p_{\text{SM}}$	$\Lambda_{\text{lim}}^+$ (TeV)	$p_{\text{SM}}$	
VV	5.0		4.7	0.28	0.021
VA	2.6	0.25	2.5	0.25	0.070
AA	3.7	0.28	2.6		0.080
X1	2.8	0.26	1.8		0.113
X2	3.1		3.4	0.28	0.056
X3	2.8		2.9	0.37	0.066
X4	4.3		4.0	0.26	0.034
X5	3.3		3.5	0.28	0.052
X6	1.7	0.16	2.8	0.27	0.105
U1	2.6	0.24	2.0		0.125
U2	3.9		4.0	0.38	0.037
U3	3.5		3.7	0.48	0.046
U4	4.8		4.4	0.32	0.025
U5	4.2		4.0	0.36	0.032
U6	1.8		2.4	0.24	0.118

**Table 3:** Values of the 95% C.L. limits ( $\Lambda_{\text{lim}}^\pm$ ) for all CI scenarios, as well as the SM probabilities,  $p_{\text{SM}}$ , for those scenarios with  $\epsilon/\Lambda_0^2 \neq 0$  (see Sect. 4). In the last column, the RMS width of the probability distribution  $p_L \propto \exp(-L(\epsilon/\Lambda^2))$  is indicated (cf. Appendix).

CI	$\Lambda_{\text{lim}}^{\pm}$ (TeV) (95% C.L.)					
	ZEUS <sup>a</sup> this study	ALEPH [9]	L3 [12] prelim.	OPAL [13]	CDF [14]	DØ [15]
VV+	4.7	6.4	3.8	4.1	3.5	4.9
VV-	5.0	7.1	5.0	5.7	5.2	6.1
AA+	2.6	7.2	5.6	6.3	3.8	4.7
AA-	3.7	7.9	3.5	3.8	4.8	5.5
X1+	1.8	—	—	—	—	3.9
X1-	2.8	—	—	—	—	4.5
X3+	2.9	6.7	4.0	4.4	—	4.2
X3-	2.8	7.4	3.4	3.8	—	5.1
X4+	4.0	2.9	2.9	3.1	—	3.9
X4-	4.3	4.5	4.8	5.5	—	4.4
X6+	2.8	—	—	—	—	4.0
X6-	1.7	—	—	—	—	4.3
U3+	3.7	—	6.1	4.1	—	—
U3-	3.5	—	4.9	5.8	—	—
U4+	4.4	—	2.1	2.3	—	—
U4-	4.8	—	2.9	3.2	—	—

<sup>a</sup> No comparison is made for scenarios for which only ZEUS sets limits: X2, X5, U1, U2, U5, U6.

**Table 4:** Lower  $\Lambda$  limits at 95% C.L. from this study compared to equivalent results from other experiments. The results of the L3 collaboration are preliminary. The X1, X3/U3, X4/U4, and X6 scenarios are denoted LL-LR, LL+RR or V0, LR+RL or A0, and RL-RR, respectively, by the LEP and Tevatron experiments. Note that CDF also provides limits for  $\mu\mu qq$  CI (not shown here) which can be combined with the  $eeqq$  limits if one assumes lepton flavor universality.

CI scenario	$\lambda_0$	$\lambda_1$ $\lambda_5$	$\lambda_2$ $\lambda_6$	$\lambda_3$ $\lambda_7$	$\lambda_4$ $\lambda_8$
VV	0.219960	-0.317192+2 -0.171440+6	0.102541+4 0.296531+6	0.559212+4 0.381829+7	-0.157739+5 0.604081+7
VA	0.245590	0.137604+1 0.684982+4	-0.977350+2 -0.160571+6	-0.345909+3 -0.532035+5	0.131860+5 0.948424+6
AA	0.241619	0.136626+2 0.549759+5	0.255357+3 -0.700729+5	-0.361006+4 -0.431092+6	0.477991+4 0.831623+6
X1	0.206150	0.700878+1 0.829875+4	0.510132+2 -0.124916+5	-0.102610+4 -0.338700+5	0.197029+4 0.571381+5
X2	0.198413	-0.113778+2 -0.100860+5	0.181979+3 -0.147490+5	0.126775+4 0.448248+5	0.163454+4 0.807606+5
X3	0.082637	-0.608908+1 -0.396591+3	0.109116+3 -0.110789+3	0.214284+3 0.692834+3	0.131258+3 0.517102+3
X4	0.327244	-0.213799+2 -0.519826+5	0.470532+3 -0.454742+5	0.356225+4 0.362723+6	0.558752+3 0.623043+6
X5	0.258595	-0.142310+2 -0.134481+5	0.218532+3 -0.960868+4	0.147937+4 0.720345+5	0.816187+3 0.103106+6
X6	0.143683	-0.486270+1 -0.623902+4	0.280939+2 -0.141521+5	0.843126+3 0.234297+5	0.235808+4 0.505643+5
U1	0.277925	0.822634+1 0.476597+4	0.581735+2 -0.472480+4	-0.708590+3 -0.158164+5	0.828391+3 0.208190+5
U2	0.086540	-0.100733+2 -0.122795+5	0.350929+3 -0.957897+4	0.100296+4 0.960528+5	0.118597+3 0.159882+6
U3	0.016648	-0.397315+1 -0.115302+2	0.241440+3 0.154464+3	0.103296+3 -0.851289+2	-0.139481+3 0.437650+3
U4	0.145224	-0.224785+2 -0.237649+5	0.824204+3 0.454907+6	0.231869+4 0.537245+5	-0.154694+5 -0.486230+7
U5	0.108391	-0.149704+2 -0.546963+4	0.498695+3 0.877442+5	0.981530+3 0.215059+3	-0.449846+4 -0.652759+6
U6	0.174813	-0.417751+1 -0.284097+4	0.981713+1 -0.650313+4	0.462709+3 0.835725+4	0.134709+4 0.172630+5

**Table 5:** Parameterizations of the functions  $L(\epsilon/\Lambda^2) - L_{\min}$  resulting from the unbinned method. For each CI scenario, the nine coefficients  $\lambda_i$  define a polynomial  $\sum_{i=0}^8 \lambda_i (\epsilon/\Lambda^2)^i$  which has been fitted to  $L(\epsilon/\Lambda^2) - L_{\min}$  in the range where  $L(\epsilon/\Lambda^2) - L_{\min} < 18$ . The notation  $x+n$  is used as a shorthand for  $x \cdot 10^n$ .

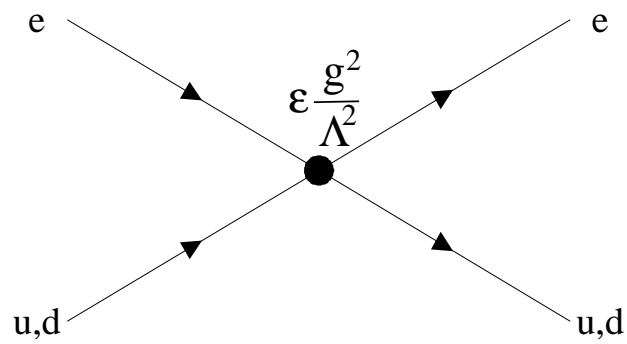


**Figure 1:** The Feynman diagram for an  $eeqq$  contact interaction.

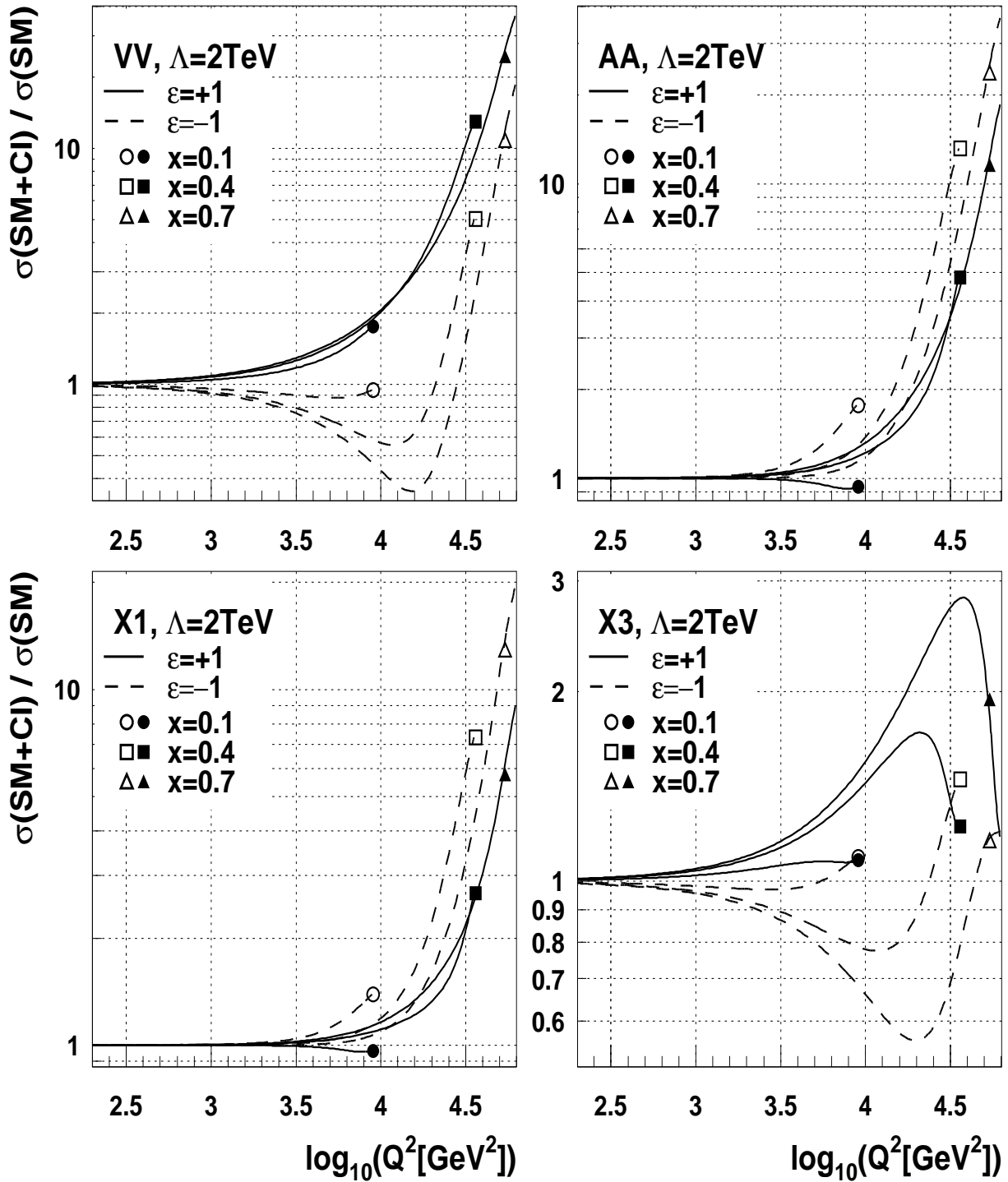


**Figure 2:** Examples of the relative influence of a CI on the NC DIS cross section  $d^2\sigma/(dx dQ^2)$  at various fixed values of  $x$ . The ratio  $(\text{SM+CI})/\text{SM}$  of differential cross sections for the scenarios VV (top left), AA (top right), X1 (bottom left) and X3 (bottom right) is plotted for  $\Lambda = 2 \text{ TeV}$ . The symbols are used only to label the different curves.

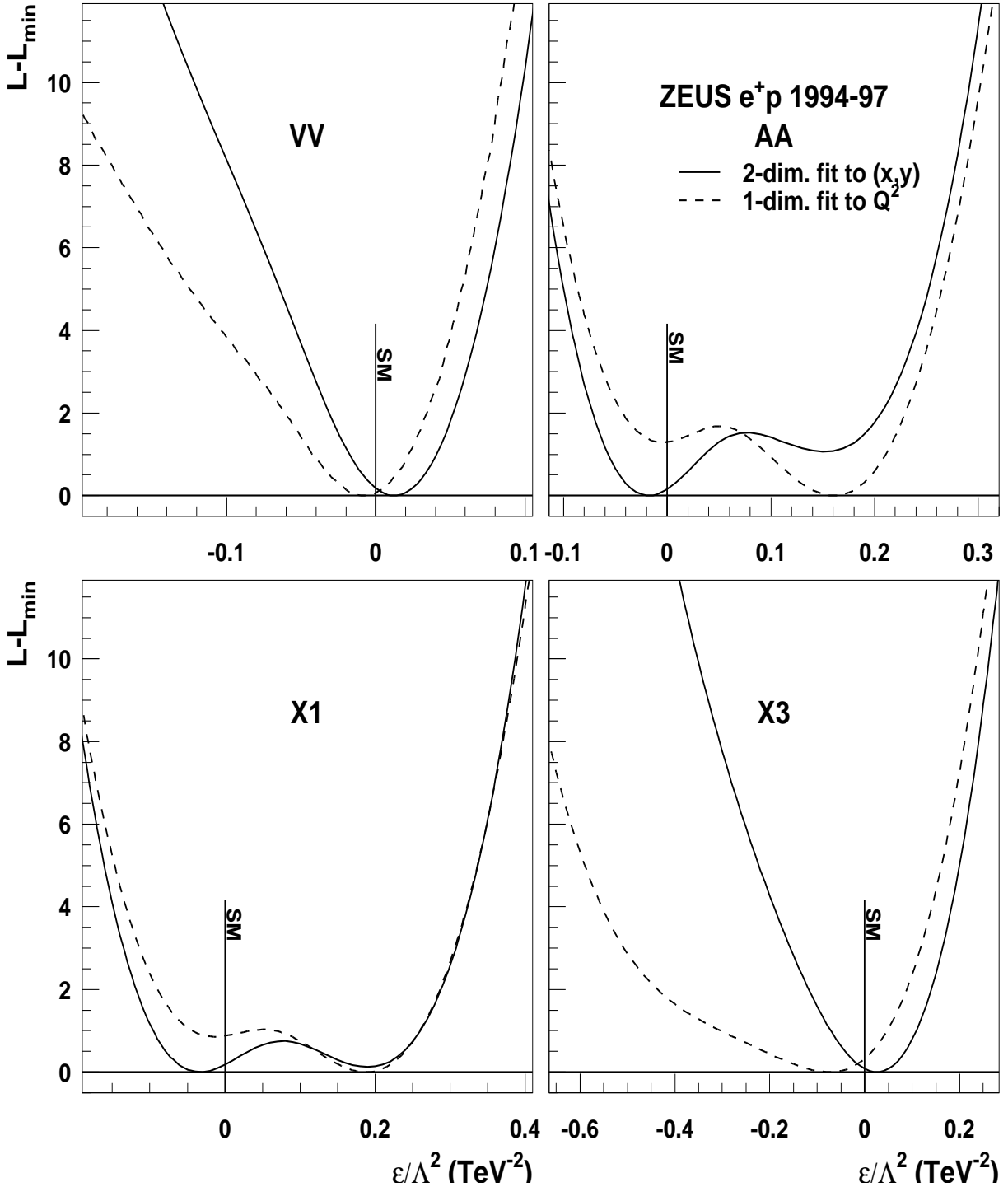


**Figure 3:** Log-likelihood as a function of  $\epsilon/\Lambda^2$  as obtained by the two methods described in Sect. 4, for the scenarios VV (top left), AA (top right), X1 (bottom left), and X3 (bottom right). For both methods, the values of  $L - L_{\min}$  are shown. Note that the two methods use different statistical approaches and, in addition, differ in their treatment of systematic effects. Each figure represents two CI scenarios ( $\epsilon = +1, \epsilon = -1$ ).

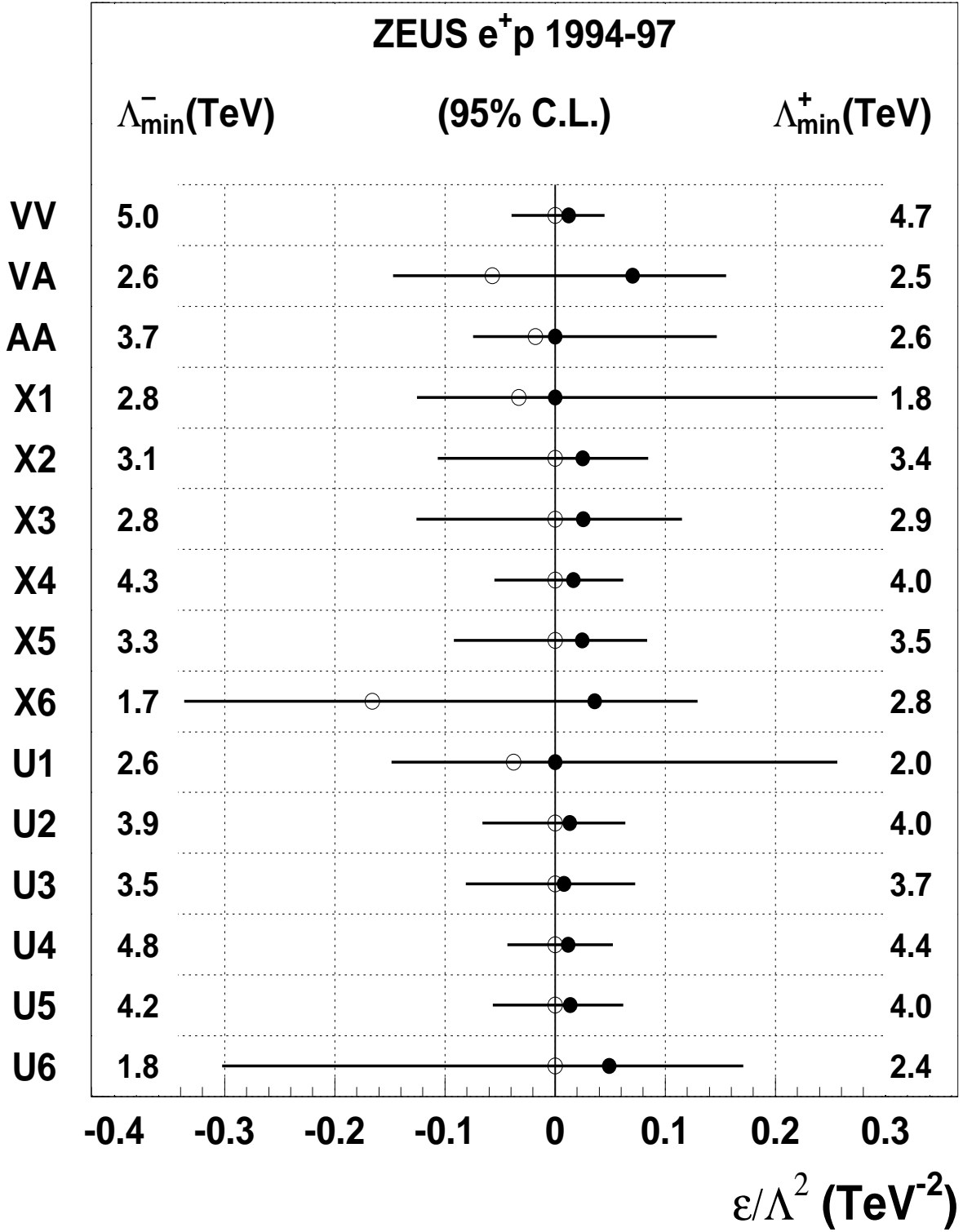


**Figure 4:** Confidence intervals of  $\epsilon/\Lambda^2$  at 95% C.L. for all CI scenarios studied in this paper (horizontal bars). The filled (open) circles indicate the positions of the log-likelihood minima,  $\epsilon/\Lambda_0^2$ , for  $\epsilon = +1$  ( $\epsilon = -1$ ). The numbers at the right (left) margin are the lower  $\Lambda$  limits for  $\epsilon = +1$  ( $\epsilon = -1$ ).

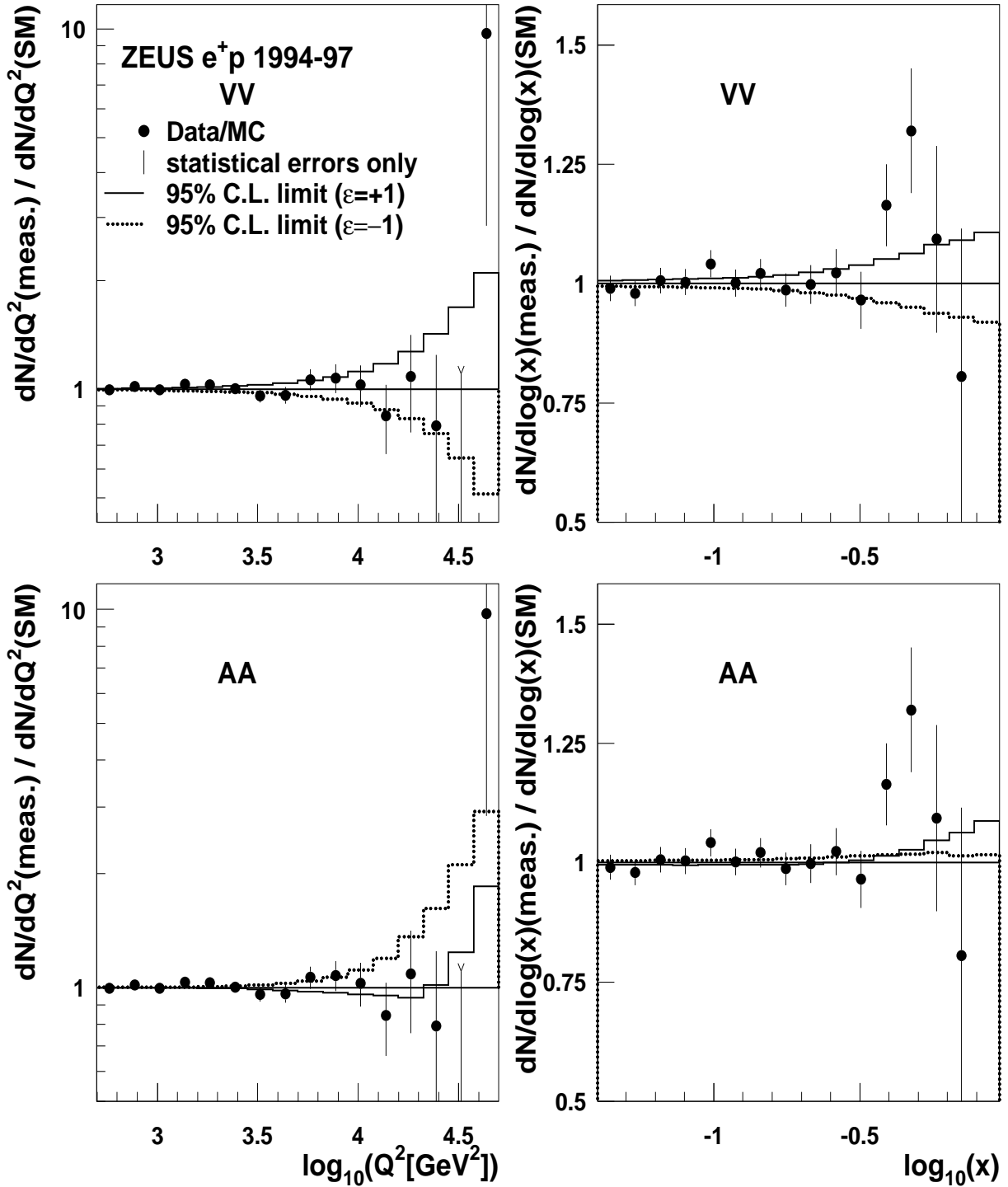


**Figure 5:** Exclusion limits on CI strengths in terms of the corresponding modification of the expected distributions of  $Q^2$  (left) and  $x$  (right) in the kinematic region used for method 1 (see Sect. 4 and Table 2). The dots represent the ratios of observed and expected numbers of events and the error bars indicate the statistical uncertainties. The histograms show the modification of this ratio for the VV (top) and AA (bottom) scenarios as obtained with the  $\Lambda_{\text{lim}}$  values given in Table 3. The solid (dotted) line corresponds to the 95% exclusion limit for  $\epsilon = +1$  ( $\epsilon = -1$ ).

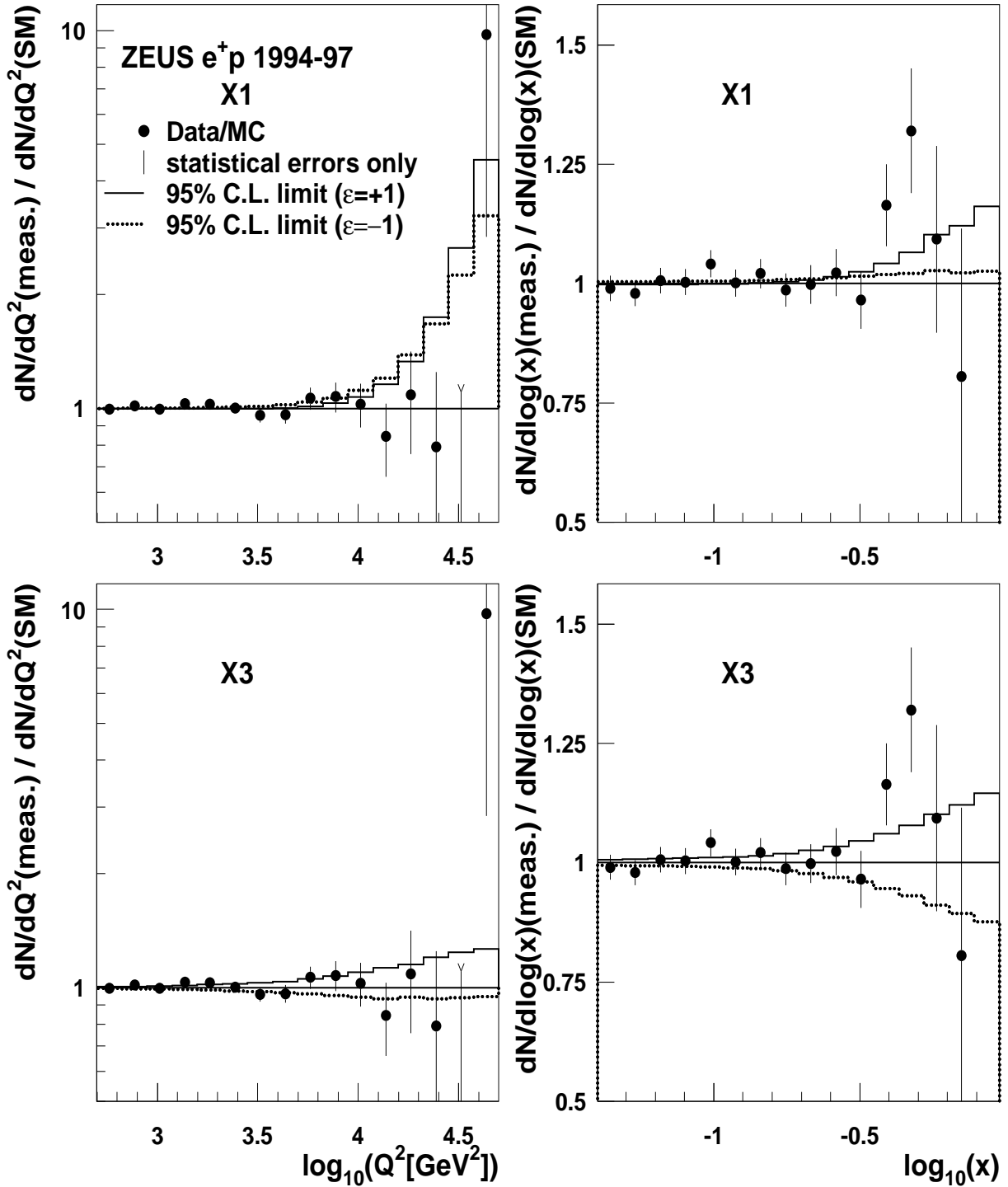


**Figure 6:** Exclusion limits on CI strengths in terms of the corresponding modification of the expected distributions of  $Q^2$  (left) and  $x$  (right) in the kinematic region used for method 1 (see Sect. 4 and Table 2). The dots represent the ratios of observed and expected numbers of events and the error bars indicate the statistical uncertainties. The histograms show the modification of this ratio for the X1 (top) and X3 (bottom) scenarios as obtained with the  $\Lambda_{\text{lim}}$  values given in Table 3. The solid (dotted) line corresponds to the 95% exclusion limit for  $\epsilon = +1$  ( $\epsilon = -1$ ).

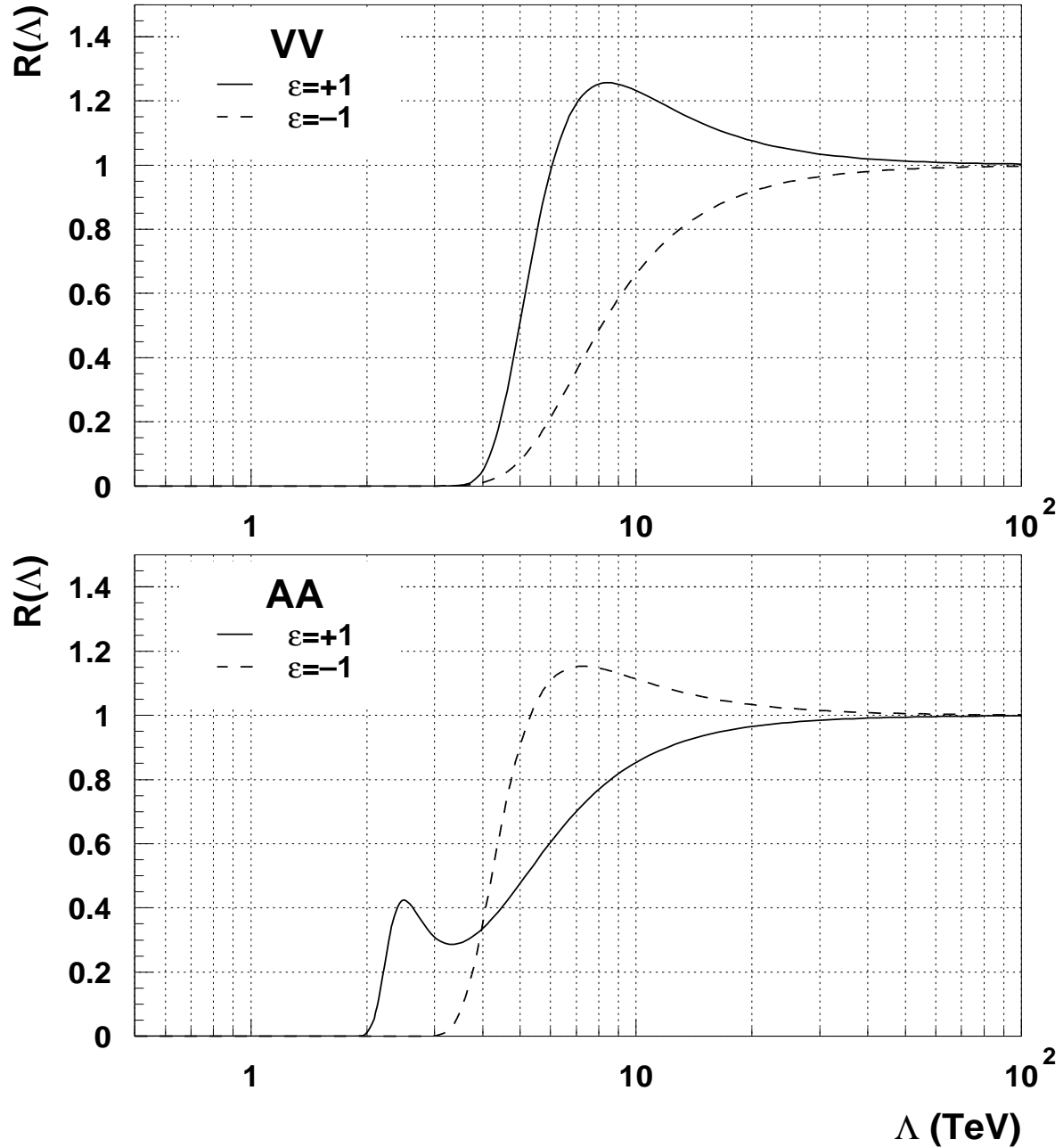


**Figure 7:** The function  $R$  defined in eq. (14) for the  $VV$  (top) and the  $AA$  (bottom) scenarios, for  $\epsilon = +1$  (solid lines), and for  $\epsilon = -1$  (dashed lines). The graphs are based on the polynomial parameterizations of Table 5.